Macromolecules
ARTICLE

Macromolecules **2010**, *43*, 6739–6748 **6739**
DOI: 10.1021/ma101062j

Effects of Polymorphism and Crystallite Size on Dipole Reorientation in Poly(vinylidene fluoride) and Its Random Copolymers

Fangxiao Guan,[†] Jing Wang,[†] Jilin Pan,[‡] Qing Wang,[‡] and Lei Zhu*[,†,§]

[†]*Polymer Program, Institute of Materials Science and Department of Chemical, Materials and Biomolecular Engineering, University of Connecticut, Storrs, Connecticut 06269-3136,* [‡]*Department of Materials Science and Engineering, Pennsylvania State University, University Park, Pennsylvania 16802, and* [§] *Department of Macromolecular Science and Engineering, Case Western Reserve University, Cleveland, Ohio 44106-7202*

Received January 2, 2010; Revised Manuscript Received July 6, 2010

ABSTRACT: Poly(vinylidene fluoride) (PVDF) and poly(VDF-*co*-hexafluoropropylene) [P(VDF−HFP)] films having different polymorphisms and crystallite sizes but a similar crystal orientation (i.e., *c*-axes parallel to the film surface) were prepared by different film processing methods. Effects of polymorphism and crystallite size on the dipole reorientation behavior and electric energy storage/release were studied by electric displacement−electric field ($D-E$) loop measurements. Experimental results suggested that coupling interactions among ferroelectric domains, which could be adjusted by different polymorphisms and/or crystallite sizes, determined dipole reorientation/switching behaviors. Note that the ferroelectric domain coupling is realized via induced compensation polarizations from the media (either amorphous or crystalline PVDF) between aligned ferroelectric domains. A high β rather than α/δ content and a large crystallite size facilitated the coupling interactions among ferroelectric domains, and thus dipoles in highly coupled ferroelectric domains could be easily polarized, resulting in a high dielectric constant and a high stored energy density. However, strong coupling interactions impeded an easy dipole reversal to the so-called antiferroelectric-like (or random) state and thus reduced the discharged electric energy due to a high remanent polarization. Instead, the film with a high β content and a small crystallite size showed the highest discharged electric energy density, suggesting that the ferroelectric domain coupling could be weakened by confining them in nanoscale crystallites. These findings provide us useful guidance to achieve optimal crystalline morphology in PVDF copolymer films for high electric energy storage applications.

Introduction

Among commercially available polymer capacitor films, poly(vinylidene fluoride) (PVDF) stands out because of its high dielectric constant[1−6] and high dc breakdown strength (~700 MV/m for ~10 μm capacitor grade films).[7−10] However, typical dielectric losses (tan δ) for α- and β-crystals, which are due to the relaxation of electric dipoles, are nearly 0.02 at 1 kHz and at ambient temperature,[11] much higher than those for current state-of-the-art dielectric capacitor films (e.g., tan $\delta \sim 0.0002$ at 1 kHz for biaxially oriented polypropylene[12]). Furthermore, relatively easy phase transformations between the paraelectric α phase and ferroelectric phases (δ-, γ-, and β-phases) at elevated electric fields[1,3] enhance the cooperative ferroelectricity in PVDF. Early polarization saturation of the ferroelectric phase at relatively low electric fields decreases the discharged energy density. Therefore, relatively high dielectric loss, large cooperative ferroelectricity, and early polarization saturation impede the practical application of PVDF as advanced dielectric films for high energy density capacitors.[7,13,14]

Modifications of the PVDF chemical structure have been pursuit to reduce its cooperative ferroelectricity in the crystals.[8,9] For example, certain amounts of bulky comonomers such as chlorotrifluoroethylene (CTFE) or hexafluoropropylene (HFP) were randomly incorporated in the PVDF main chain to reduce the crystallite size. The corresponding P(VDF−CTFE) or P(VDF−HFP) copolymers therefore exhibited the relaxor-like ferroelectricity and achieved a high discharged energy density of 17−25 J/cm^3 at ~600 MV/m.[8,9] The high energy density was explained by a broadened and reversible $\alpha \leftrightarrow \beta$ phase transformation due to the existence of nanodomains in PVDF crystals.[15] Furthermore, a low loss dielectric polymer, polystyrene (PS), was grafted onto P(VDF−CTFE) main chains using atom transfer radical polymerization.[16] After PVDF crystallization, PS formed a confining layer surrounding the PVDF lamellar crystals. As a result, less induced compensation polarization at the crystalline/amorphous interfaces and/or space charge[17,18] was accumulated in the sample comparing to pure PVDF, and a much faster discharge speed and a lower dielectric loss were achieved.

To design and develop better ferroelectric materials for high electric energy storage with low losses, which including dielectric loss at low fields, conduction[19] and ferroelectric losses at high fields, it is important for us to understand the fundamental physics of ferroelectric domain nucleation and growth, ferroelectric domain size, coupling among ferroelectric domains, competition between polarization and depolarization fields, dipole switching, crystal orientation, polymorphism, and phase transformations in ferroelectric materials. Recently, anisotropic dielectric and ferroelectric properties due to the anisotropic orientational polarizability in P(VDF−HFP) random copolymer films with different crystal orientations were studied at both low and high electric fields.[20] When PVDF *c*-axes oriented perpendicular to the electric field, CH_2CF_2 dipoles could easily respond to the external electric field, and thus high maximum and remanent polarizations and a low dipole switching field were observed. This resulted in high dielectric constants (ca. 10−12 at 1 kHz) at low fields and high electric energy densities at high fields. When PVDF crystal *c*-axes oriented parallel to the electric field, CH_2CF_2 dipoles could not easily respond to the electric field,

*Corresponding author: e-mail lxz121@case.edu; Tel (216)368-5861.

Published on Web 07/23/2010

Table 1. α and β Contents and Estimated Average Crystallite Sizes for α- and β-Crystals in Films A−E Processed by Different Methods

films	processing method	$T_{stretch}$ (°C)	crystallinity (wt %)[a]	T_m (°C)[a]	α (wt %)[b]	β (wt %)[b]	$D_{(110)\alpha}$ (nm)[b]	$D_{(110/200)\beta}$ (nm)[b]
A	biax. stretched		49.4	176	27.5	19.6	37	25
B	hot-pressed, uniax. stretched	90	32.2	143	18.2	30.6	14	11
C	hot-pressed, uniax. stretched	130	35.6	133	32.9	7.3	19	16
D	solution-cast, uniax. stretched							
⊥[c]		60	43.3	146	14.1	0	23	
∥[d]		60	43.3	146	21.1	2.7	11	10
E	solution-cast, uniax. stretched							
⊥[c]		110	41.1	146	9.6	0	25	
∥[d]		110	41.1	146	22.3	9.1	13	12

[a] Determined by differential scanning calorimetry (DSC). [b] Determined by 2D wide-angle X-ray diffraction (WAXD). [c] PVDF crystalline lamellae lie flat-on in the film with their *c*-axes parallel to the film normal. [d] PVDF crystalline lamellae lie transverse in the film with their *c*-axes parallel to the drawing direction.

and a relatively low dielectric constant (ca. 5.6 at 1 kHz) and a low energy density were observed.

In this work, we continued to investigate effects of polymorphism (α/δ- versus β-forms) and crystallite size on dipole reorientation/switching and electric energy storage/release in a biaxially oriented PVDF film and a series of uniaxially oriented P(VDF−HFP) random copolymer films. To avoid possible interference from different crystal orientations, all films were processed by mechanical stretching to obtain a similar orientation, i.e., *c*-axes oriented parallel to the film surface. Dipole switching and electric energy storage/release were studied by electric displacement−electric field (*D*−*E*) loop measurements. The objective is to understand how the coupling interactions among ferroelectric domains and competition between polarization and depolarization fields affect the dipole reorientation behavior and stored/released electric energy densities for high energy density capacitor applications.

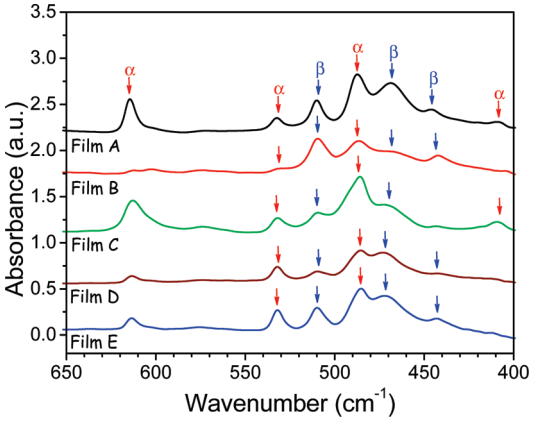

Figure 1. Differential FTIR absorption spectra for films A−E. Curves are offset for clarity.

Experimental Section

Materials. The biaxially oriented PVDF film (12 μm, film A) was provided by courtesy of General Atomics (San Diego, CA). P(VDF−HFP)-96/4 resin (pellets) was purchased from Aldrich, which contained 4 mol % HFP comonomer as determined by fluorine nuclear magnetic resonance (^{19}F NMR). Its number-average molecular weight is 130 000 g/mol, and its weight-average molecular weight is 400 000 g/mol. Tetrahydrofuran (THF, Aldrich, HPLC grade) was used as received without further purification.

Film Fabrication and Processing. Film HP with a thickness around 80−100 μm was prepared by hot-pressing the P(VDF−HFP)-96/4 resin at 240 °C followed by immediate quenching into ice/water. Films B and C with thicknesses around 20 μm were prepared by uniaxial stretching (~500% extension ratio) of the film HP at 90 and 130 °C, respectively. Film SC with a thickness around 50 μm was prepared by slow solution-casting from 4 wt % solution of P(VDF−HFP) in THF at room temperature. Films D and E with thicknesses around 8 μm were prepared by uniaxial stretching (~650% extension ratio) of film SC at 60 and 110 °C, respectively. Different processing methods for films A−E are summarized in Table 1.

Instrumentation and Characterization. Two-dimensional (2D) wide-angle X-ray diffraction (WAXD) experiments were performed on an Oxford Xcalibur diffractometer with an ONYX CCD area detector. The X-ray wavelength was Cu Kα 0.1542 nm. One-dimensional (1D) WAXD profiles were obtained by integrating the corresponding 2D WAXD images. The *d*-spacing was calibrated using silver behenate with the first-order reflection at a scattering vector $q = 1.076\ nm^{-1}$, where $q = (4\pi \sin\theta)/\lambda$ with θ being the half scattering angle. Fourier transform infrared (FTIR) was performed on a Nicolet Magna 560 FTIR spectrometer. Differential FTIR spectra were obtained by subtracting FTIR spectra with that for the P(VDF−HFP) in the melt at 180 °C.[21] Differential scanning calorimetry (DSC) thermograms were obtained using a TA Instruments Q20 DSC at a heating rate of 10 °C/min.

Polarization hysteresis loops at room temperature were collected using a modified Sawyer−Tower circuit at 10 Hz.[9] Gold electrodes were sputtered onto both surfaces of the film with a thickness around 50 nm. The gold electrode area was ca. 0.0531 cm^2 for the *D*−*E* loop measurements.

Results

Characterization of Crystalline Morphology in Various PVDF Films. Polymorphism, crystal orientation, and crystallite size in various PVDF films were studied by differential FTIR and WAXD techniques. Figure 1 shows differential FTIR spectra for films A−E. Typical α-form absorption bands were observed at 614, 532, 486, and 410 cm^{-1}, and typical β-form absorption bands were found at 510, 472, and 442 cm^{-1}. Detailed peak assignments of these FTIR absorption bands for α- and β-forms can be found in previous reports.[20,22] Judging from the intensities at 532 cm^{-1} for the α-form and 510 cm^{-1} for the β-form, the β content should decrease in the order of films B > A > E ≈ C > D. Note that the absorption bands at 532 and 510 cm^{-1} are both assigned to the $\delta(CF_2)$ stretching (perpendicular to the chain direction) for the α- and β-forms, respectively.[22] Therefore, their intensities can be directly used to qualitatively estimate the relative α and β contents in the films.

Although differential FTIR spectra showed distinct β- and α-form absorption bands, the absolute α and β contents could not be quantitatively determined because the absolute absorption coefficients were not readily available and different α and β crystal orientations further complicated the absolute infrared absorption. Therefore, the α and β contents and crystal orientations in films A−E were studied by 2D WAXD (see Figure 2). The incident X-ray beam was

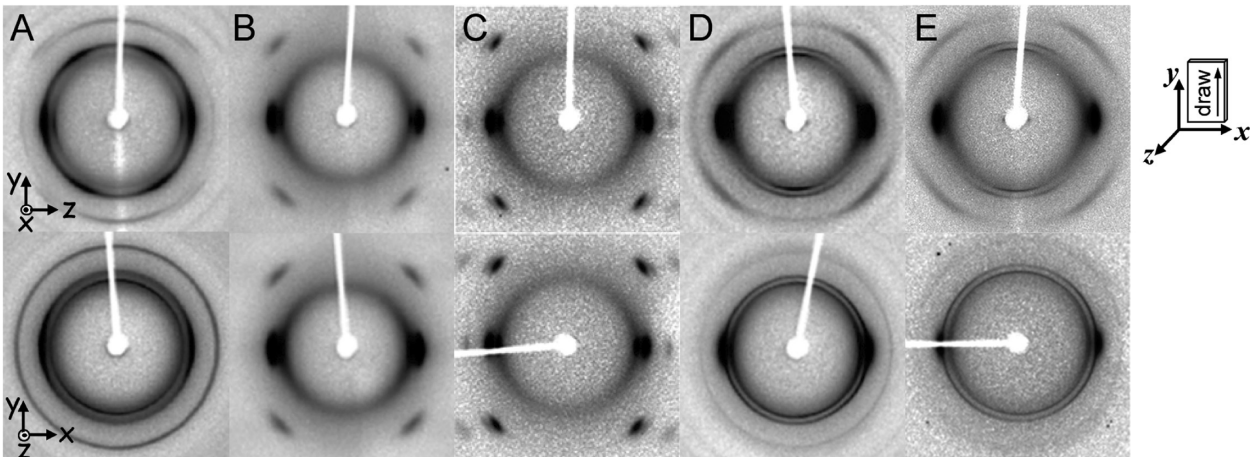

Figure 2. 2D WAXD patterns along the *x* (top) and *z* (bottom) directions for films A−E. The schematic on the right shows that for uniaxially drawn films, the drawing direction is along the *y*, the normal direction is along the *z*, and the transverse direction is the *x*.

directed along the *x* (transverse to the drawing direction) and the *z* (normal to the film) directions, respectively. For the biaxially oriented film A, PVDF chains in the crystalline lamellae oriented primarily along the *y* (i.e., machine) and *x* (i.e., transverse) directions, respectively, because the $(020)_\alpha$, $(110)_\alpha$, and $(110)_\beta/(200)_\beta$ reflections were along the *z*-direction in the *x* 2D WAXD pattern (top panel of Figure 2A). Note that the crystal orientation was much better and the intensity of oriented reflections was much stronger in the *x* 2D WAXD pattern than in the *z* 2D WAXD pattern, suggesting that the draw ratio along the *y* direction (i.e., machine direction) must be greater than that along the *x* direction (i.e., transverse direction). Therefore, more PVDF lamellar crystals oriented transverse to the *y* direction than transverse to the *x* direction. This is typical for tenter-line processed biaxially oriented films.[23]

For hot-pressed and stretched films B and C, PVDF chains in the crystalline lamellae oriented exclusively along the *y* direction because $(100)_\alpha$, $(020)_\alpha$, and mixed $(110)_\alpha/(110)_\beta/(200)_\beta$ reflections appeared in the horizontal *z* and *x* directions in the *x* (Figure 2B) and *z* (Figure 2C) 2D WAXD patterns, respectively.[20]

For solution-cast and stretched films D and E, two types of crystal orientations were observed in the same sample.[20] One was a perpendicular orientation, namely, *c*-axes in pre-existing flat-on PVDF crystals (crystallized from THF solution during the slow solution-casting process) oriented normal to the film. This crystal orientation was evidenced by sharp $(100)_\alpha$, $(020)_\alpha$, and $(110)_\alpha$ reflections along the *y*-direction in the *x* 2D WAXD pattern in the top panels of parts D and E of Figure 2, respectively. The other was parallel orientation, namely, *c*-axes in the (transformed) transverse PVDF crystals aligned parallel to the drawing direction.[24,25] This crystal orientation was evidenced by broad $(100)_\alpha$, $(020)_\alpha$, $(110)_\alpha$, and $(110)_\beta/(200)_\beta$ reflections along the horizontal *x*- and *z*-directions in the *z* and *x* 2D WAXD patterns in the bottom panels of parts D and E of Figure 2, respectively. A detailed discussion about these crystal orientations can be found in ref20.

The α and *β* contents in films A−E were estimated by 1D WAXD profiles in Figure 3 for films A−C and Figure 4 for films D and E, respectively. To avoid the interference from different crystal orientations, 1D WAXD profiles were integrated from the 2D WAXD patterns when the X-ray beam was directed along the *x*-direction because equal reflection probabilities for the (*hk*0) reflections in both flat-on and transverse α- and *β*-crystals could be assumed as long

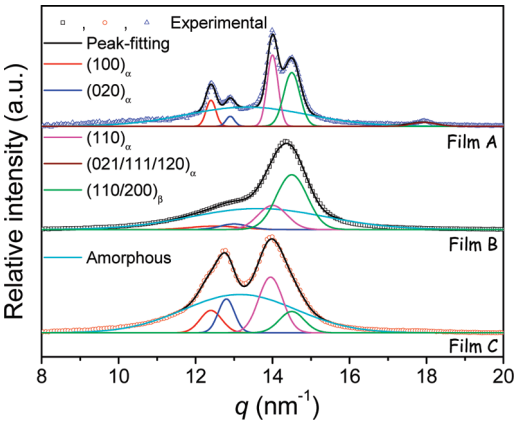

Figure 3. 1D WAXD profiles from integration of the *x*-direction 2D WAXD patterns in top panels of Figure 1A−C.

as the crystals had a random orientation around the drawing direction. (This was exactly observed experimentally, but results are not shown here.) In addition, the crystallinities obtained from these integrated 1D WAXD profiles generally matched those determined by DSC (see Table 1). Therefore, we believe that these integrated 1D WAXD results should be reliable to compare the relative *β* content. In these 1D WAXD profiles in Figures 3 and 4, the α-crystal reflections, $(100)_\alpha$, $(020)_\alpha$, and $(110)_\alpha$, were seen at 12.45, 12.95, and 14.05 nm^{-1}, respectively. The *β*-crystal reflections, $(110)_\beta/(200)_\beta$, was seen at 14.5 nm^{-1}. The actual contents of α- and *β*-crystals were directly determined by the α- and *β*-crystallinity from the peak-fitting results in Figure 3 for films A−C, Figure 4A for film D, and Figure 4B for film E (see Table 1). There were 19.6% *β*- and 27.5% transverse α-crystals in film A, 30.6% *β*- and 18.2% transverse α-crystals in film B, and 7.3% *β*- and 32.9% transverse α-crystals in film C. In film D, there were 21.1% flat-on α-crystals and 2.7% *β*- and 14.1% transverse α-crystals. In film E, there were 9.6% flat-on α-crystals and 9.1% *β*- and 22.3% transverse α-crystals.

To study the effect of average crystallite size, the apparent crystallite sizes along $[110]_\alpha$ $[D_{(110)\alpha}]$ and $[110/200]_\beta$ $[D_{(110/200)\beta}]$ directions were calculated from the Scherrer equation: $D_{hkl} = (K\lambda)/(\beta_{hkl} \cos \theta)$, where, D_{hkl} is the mean crystallite size along the [*hkl*] direction, *K* is the shape factor (a value of 0.94 is used in this case[26]), λ is the wavelength, and β_{hkl} is the pure line breadth [or the full width at half-maximum for the (*hkl*) diffraction]. The results are summarized in Table 1.

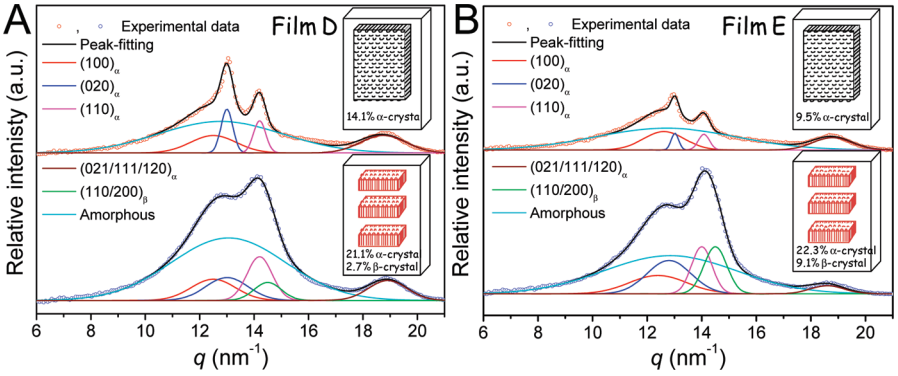

Figure 4. 1D WAXD profiles for the solution-cast and stretched films (A) D and (B) E obtained by integration along the *y*- (top) and the *z*- (bottom) directions, respectively, when the X-ray beam is directed along the *x*-direction. The integration angle is ca. 50° around the *y*- and *z*-directions, respectively.

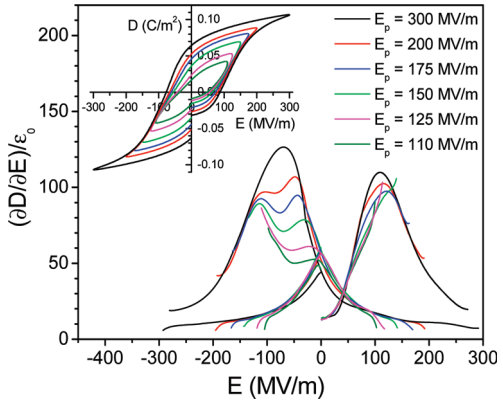

Figure 5. $(\partial D/\partial E)/\varepsilon_0$ as a function of the electric field for film A, and the inset shows the corresponding bipolar $D-E$ hysteresis loops.

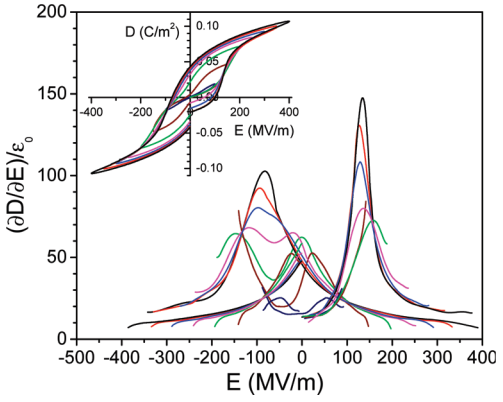

Figure 6. $(\partial D/\partial E)/\varepsilon_0$ as a function of the electric field for film B, and the inset shows the corresponding bipolar $D-E$ hysteresis loops.

Biaxially oriented film A had the largest crystallite size among all samples—36.9 nm along $[110]_\alpha$ and 24.6 nm along $[110/200]_\beta$—because it was a homopolymer processed by a tenter line. In films B and C, the α- and β-crystallite sizes substantially decreased because of the existence of HFP comonomers, fast quenching into ice water from the melt, and large stretching ratio: 13.7 nm along $[110]_\alpha$ and 11.4 nm along $[110/200]_\beta$ in film B; 19.0 nm along $[110]_\alpha$ and 15.5 nm along $[110/200]_\beta$ in film C. In film D, the crystallite sizes along the $[110]_\alpha$ direction were 22.7 and 10.7 nm for the preexisting flat-on and transformed transverse α-crystals, respectively. The crystallite size along the $[110/200]_\beta$ direction was 10.2 nm for the transformed transverse β-crystals. In film E, the crystallite sizes along the $[110]_\alpha$ direction were 24.6 and 13.4 nm for the preexisting flat-on and the transformed transverse α-crystals, respectively. The crystallite size along the $[110/200]_\beta$ direction was 11.8 nm for the transformed transverse β-crystals.

Ferroelectric Properties at High Electric Fields. From the above morphology studies, PVDF films with different polymorphisms and crystallite sizes were obtained. From our previous study, the ferroelectric response from flat-on α-crystals was much less than that from transverse α/δ- and/or β-crystals because CH_2CF_2 dipoles oriented in a plane perpendicular to the electric field and could not easily respond to the external field. As such, we might be able to ignore the contribution from the preexisting flat-on α-crystals in films D and E and then investigated the effects of polymorphism and crystallite size on the ferroelectric properties and electric energy storage using $D-E$ loop measurements. Bipolar electric field was applied as a sinusoidal waveform having a frequency of 10 Hz. For linear dielectric materials, the relative dielectric constant (ε_r) is determined by the electric displacement as $\varepsilon_r = (\partial D/\partial E)/\varepsilon_0$. However, this relationship is generally invalid for a ferroelectric (or nonlinear) material such as PVDF because the electric displacement at high electric fields changes irreversibly with the electric field.[27] Note that the electric displacement primarily accounts for the dipole orientation (or polarization), while the dielectric constant reflects the motion (or the rate of change) of these dipoles. D and ε_r are not independent but often correlate with each other. Although the above equation cannot be directly used to calculate the field-dependent dielectric constant for nonlinear materials, it was observed experimentally that $(\partial D/\partial E)/\varepsilon_0$ qualitatively correlated with ε_r as a function of the electric field.[20,27,28] In our $D-E$ loop measurements, unfortunately the field-dependent $\varepsilon_r(E)$ could not be directly obtained from the circuit. Therefore, $(\partial D/\partial E)/\varepsilon_0$ was used to qualitatively correlate with the relative dielectric constant at high electric fields for these PVDF and P(VDF−HFP) films.

The $(\partial D/\partial E)/\varepsilon_0$ as a function of the electric field for films A−E are shown in Figures 5−9, where the corresponding $D-E$ loops are shown as insets. For film A, $(\partial D/\partial E)/\varepsilon_0$ showed a maximum at 130 MV/m upon the forward poling after the poling field reached > 175 MV/m (Figure 5). At this peak electric field, the switching (or poling) rate of the dipoles reached a maximum. The magnitude of this peak field indicated how easy the dipoles could be aligned by the electric field; the lower the peak field, the easier the dipoles could be oriented.

When the poling field was reverted to the opposite direction, the $D-E$ loops appeared to have a propeller shape, and

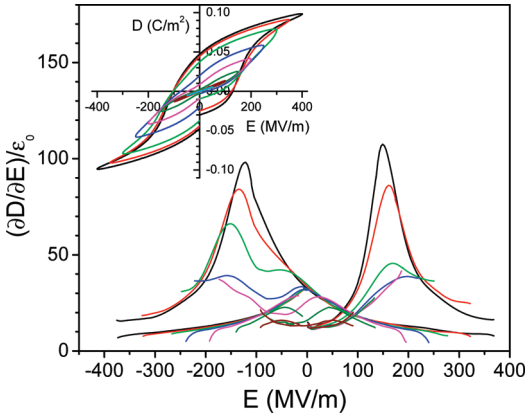

Figure 7. $(\partial D/\partial E)/\varepsilon_0$ as a function of the electric field for film C, and the inset shows the corresponding bipolar $D-E$ hysteresis loops.

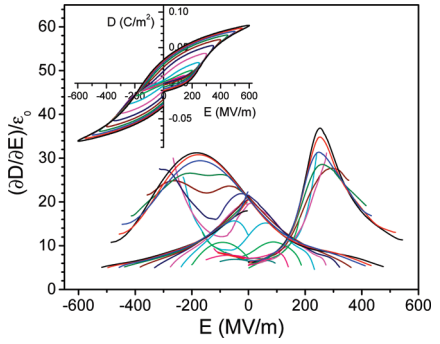

Figure 8. $(\partial D/\partial E)/\varepsilon_0$ as a function of the electric field for film D, and the inset shows the corresponding bipolar $D-E$ hysteresis loops.

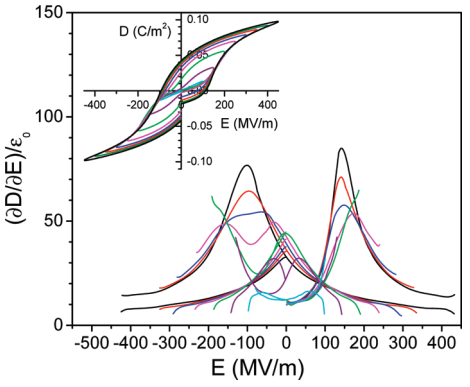

Figure 9. $(\partial D/\partial E)/\varepsilon_0$ as a function of the electric field for film E, and the inset shows the corresponding bipolar $D-E$ hysteresis loops.

two maxima in the reverse poling $(\partial D/\partial E)/\varepsilon_0$ curves were observed, suggesting a two-step dipole reversal process upon reverse poling, as reported before.[20,27,29−32] However, the fundamental mechanism for the two-step dipole reversal process in ferroelectric polymers still needs further clarification. The first dipole reversal process took place with a $(\partial D/\partial E)/\varepsilon_0$ peak at low reverse poling fields and could be explained by an antiferroelectric-like behavior; namely, part of the polarized dipoles reverted, resulting in a nearly zero net dipole moment in the sample.[27,30,31] The second dipole reversal process occurred with another $(\partial D/\partial E)/\varepsilon_0$ peak at high reverse poling fields, and the dipoles started to fully reverted to the opposite direction. Obviously, the reverse poling process depended closely on the prior forward poling process. For low forward poling fields (e.g., 110−125 MV/m), there was one $(\partial D/\partial E)/\varepsilon_0$ peak observed upon reverse poling, which could be attributed to the first-step dipole reversal (e.g., −11 MV/m for a forward poling field of 110 MV/m and −21 MV/m for a forward poling field of 125 MV/m). Only part of the second peak was observed at higher reverse poling fields because the necessary reverse poling field for complete dipole reversal was not yet reached. For medium forward poling fields (e.g., 150−200 MV/m), two $(\partial D/\partial E)/\varepsilon_0$ peaks were observed, corresponding to two steps of dipole reversal, respectively. For example, the first-step dipole reversal to the antiferroelectric-like state occurred at −32, −45, and −48 MV/m for the forward poling field being 150, 175, and 200 MV/m, respectively. The complete (i.e., the second-step) dipole reversal occurred at −115, −111, and −103 MV/m for the forward poling field of 150, 175, and 200 MV/m, respectively. Obviously, the higher the forward poling field, the more negative the first-step dipole reversal field and the less negative the second-step dipole reversal field. These results indicated that the first-step dipole reversal became more difficult and the second-step dipole reversal became easier, when the forward poling field gradually increased. Finally, for a high poling field (e.g., 300 MV/m), the two $(\partial D/\partial E)/\varepsilon_0$ peaks merged and polarized dipoles started to directly revert to the opposite direction at −70 MV/m.

Films B−E showed similar behaviors as that of film A (see Figures 6−9), except for different $(\partial D/\partial E)/\varepsilon_0$ peak values and peak fields. The $(\partial D/\partial E)/\varepsilon_0$ peak values as a function of the forward and reverse poling fields are summarized in Figure 10 for films A−E. During the forward poling process, $(\partial D/\partial E)/\varepsilon_0$ peak values for all films increased with increasing the poling field due to an increased dipole orientation rate within the same voltage rising time (i.e., within 25 ms). The β content increased in an order of films D < E ≈ C < A < B (see Table 1). From the right panel in Figure 10, the $(\partial D/\partial E)/\varepsilon_0$ peak values at a given poling field generally increased with the β content in the films. This is understandable because the β-form had a higher dipole moment than the α/δ-form per chain per repeat unit. (Note that upon poling at an electric field greater than 100 MV/m the α-form starts to transform into the δ-form.[1,3] Since it is not trivial to unambiguously differentiate the α-form from the δ-form especially when the crystallite size is small, we will simply refer the low-field phase as the α/δ-form in this study.) However, there were a few exceptions. First, film C exhibited higher $(\partial D/\partial E)/\varepsilon_0$ peak values than film E above 250 MV/m, even though it had a slightly lower β content (7.3%) than film E (9.1%). This could be attributed to the α → β phase transformation induced by electric poling above 250 MV/m for film C, resulting in a final β content of 17.3%, as reported previously.[20] Note that no obvious phase transformation was observed upon high field poling for films D and E.[20] Second, film A had higher $(\partial D/\partial E)/\varepsilon_0$ peak values than film B below 300 MV/m, although the β content for film A (19.6%) was lower than that for film B (30.6%). From Table 1, film A had much larger lateral crystallite sizes (36.9 nm for $D_{(110)\alpha}$ and 24.6 nm for $D_{(110/200)\beta}$) than film B (13.7 nm for $D_{(110)\alpha}$ and 11.4 nm for $D_{(110/200)\beta}$). Therefore, it is reasonable for us to conclude that in addition to polymorphism, crystallite size also affected the ferroelectric behavior; the larger the crystallite size, the more cooperativeness of dipoles[33] and thus the higher the ferroelectric responses.

Upon reverse poling (the left panel of Figure 10), similar trends were generally observed; the higher the β content, the higher the $(\partial D/\partial E)/\varepsilon_0$ peak values except for films A and C. For film A, higher $(\partial D/\partial E)/\varepsilon_0$ peak values were observed as compared to film B, even though it has less β content. This again could be attributed to its larger lateral crystallite sizes.

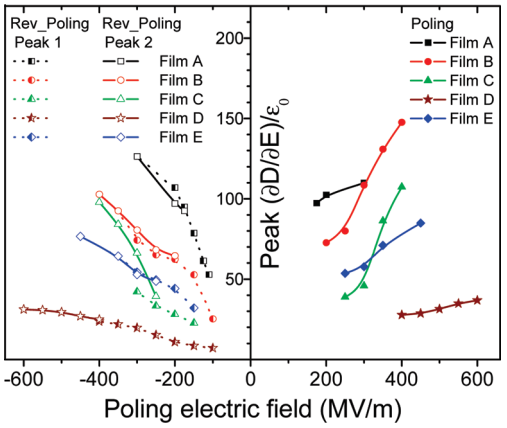

Figure 10. $(\partial D/\partial E)/\varepsilon_0$ peak values as a function of positive (right panel) and reverse (left panel) poling fields for films A−E.

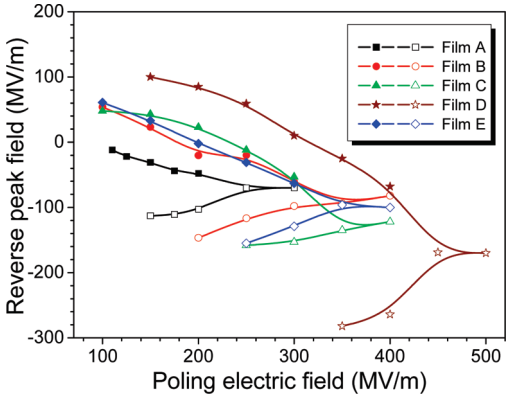

Figure 11. $(\partial D/\partial E)/\varepsilon_0$ peak field as a function of prior forward poling field during the subsequent reverse poling processes for films A−E. The first-step dipole reversal is represented by solid symbols, and the second-step dipole reversal is represented by open symbols.

For film C during the second step dipole reversal, $(\partial D/\partial E)/\varepsilon_0$ peak values were higher than those for film E at < -300 MV/m. Again, this could be attributed to the $\alpha \rightarrow \beta$ phase transformation induced by electric poling above 250 MV/m during the forward poling process for film C.

While the $(\partial D/\partial E)/\varepsilon_0$ peak value indicates how fast dipoles are polarized, the $(\partial D/\partial E)/\varepsilon_0$ peak field indicates how easily the dipoles can be polarized. Figure 11 summarizes the $(\partial D/\partial E)/\varepsilon_0$ peak field during the reverse poling process as a function of the prior forward poling field for films A−E. Two-step dipole reversals were observed for relatively low forward poling fields, and they merged into one reversal process at high enough forward poling fields. Generally speaking, with increasing the β content at a given forward poling field, the $(\partial D/\partial E)/\varepsilon_0$ peak field for the first-step dipole reversal decreased (or moved toward more negative), while the $(\partial D/\partial E)/\varepsilon_0$ peak field for the second-step dipole reversal increased (or moved toward more positive). Therefore, we conclude that the first-step dipole reversal due to the antiferroelectric-like behavior became more difficult, while the second-step dipole reversal became easier when the β content increased.

An exception was observed for the dipole reversals in film A as compared to those in film B. The $(\partial D/\partial E)/\varepsilon_0$ peak field for the first-step dipole reversal was higher and the $(\partial D/\partial E)/\varepsilon_0$ peak field for the second-step dipole reversal was lower at a given forward poling field, even though the β content in film A was lower than that in film B. Again, this could be attributed to the crystallite size effect. When the lateral crystallite size was large, the coupling among ferroelectric domains was strong, and thus the first-step dipole reversal became difficult and the second-step dipole reversal became easy in film A.

Comparing films C and E, the $(\partial D/\partial E)/\varepsilon_0$ peak fields for the first-step dipole reversal were similar when the prior forward poling field was below 300 MV/m. However, the $(\partial D/\partial E)/\varepsilon_0$ peak fields for the second-step dipole reversal in film C appeared at more negative fields than those in film E, when the prior poling field was above 250 MV/m. This could again be attributed to the $\alpha \rightarrow \beta$ phase transformation above 250 MV/m in film C,[20] and thus the complete dipole reversal became more difficult due to the higher β content.

Electric Energy Storage and Discharge during Bipolar Switching. The charged and discharged electric energy densities (U_e) were directly integrated from the bipolar $D-E$ loops in the insets of Figures 5−9, and results are shown in Figure 12A,B. The loss is defined as $1 - U_e$(discharged)/U_e(charged), which includes both ferroelectric and conduction losses during bipolar switching.[9,19] The results are shown in Figure 12C. From Figure 12A, the stored U_e increased with increasing the β content and the lateral crystallite or combination thereof. Note that the curves in Figure 12A had similar shapes and trends as those in the right panel of Figure 10 for forward poling, indicating that the poling of dipoles in PVDF films was directly responsible for the electric energy storage during charging. However, the discharged U_e in Figure 12B showed different electric field dependence. The higher the β content and the smaller lateral crystallite sizes, the higher discharged U_e (see the discharged U_e for film B in Figure 12B). Moreover, the β-crystals were responsible for high losses between 100 and 300 MV/m for films A−C and E as compared to film D (Figure 12C). Note that for film B the decrease of loss by the small lateral crystallite size was more significant than the increase of loss by the high β content. Above 400 MV/m, film B had the lowest loss among all films. Therefore, the loss caused by β-crystal at high electric fields can be effectively reduced by confining and decoupling the ferroelectric domain in small (or nanosized) crystals. Note that the losses at 400 MV/m from unipolar switching for films C and E ranged between 37% and 44%,[20] lower than those from bipolar switching (63−68%) at the same electric field, indicating that PVDF-based capacitor films perform better under dc rather than ac conditions. Finally, more than 30% loss in monolithic PVDF-based films is impractical for real-world applications. Either new materials[16,34] or technologies (e.g., multilayer films[35]) are desired for high energy density and low loss dielectric film capacitors.

Discussion

The above results can be explained by the poling mechanism in terms of ferroelectric domain coupling and the competition between polarization and depolarization fields, as demonstrated in parts A and B of Figure 13, respectively. Figure 13A shows a simple serial model with a ferroelectric PVDF crystal sandwiched between two amorphous PVDF layers. Upon the application of an external electric field (E), dipoles in ferroelectric PVDF crystals will orient along the external field, thus creating a local depolarization field (E_{depol}) as shown in Figure 13A:[36,37]

$$E_{depol} = \frac{P_{in}}{\varepsilon_0} \quad (1)$$

where P_{in} is the polarization in the PVDF crystal induced by aligned dipoles and ε_0 the vacuum permittivity. Because E_{depol}

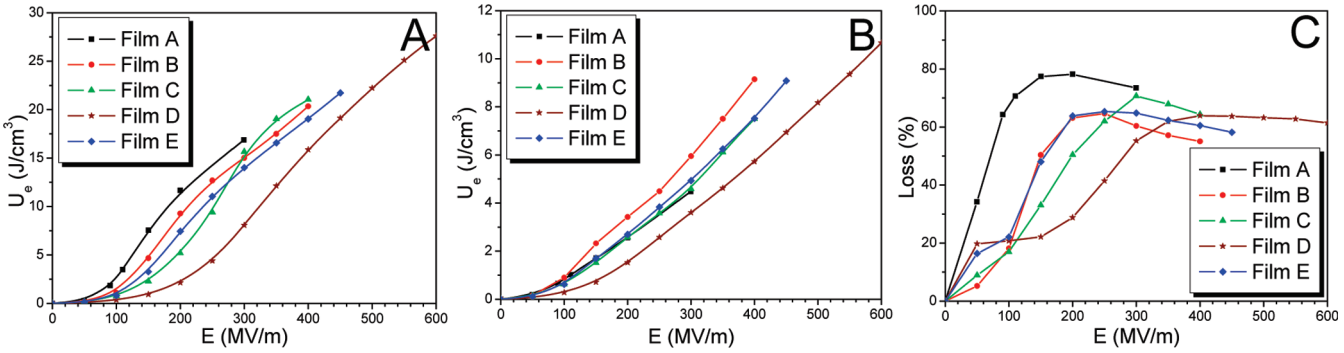

Figure 12. (A) Charged and (B) discharged energy densities and (C) loss as a function of the poling electric field obtained from bipolar $D-E$ loops in the insets of Figures 5−9 for films A−E.

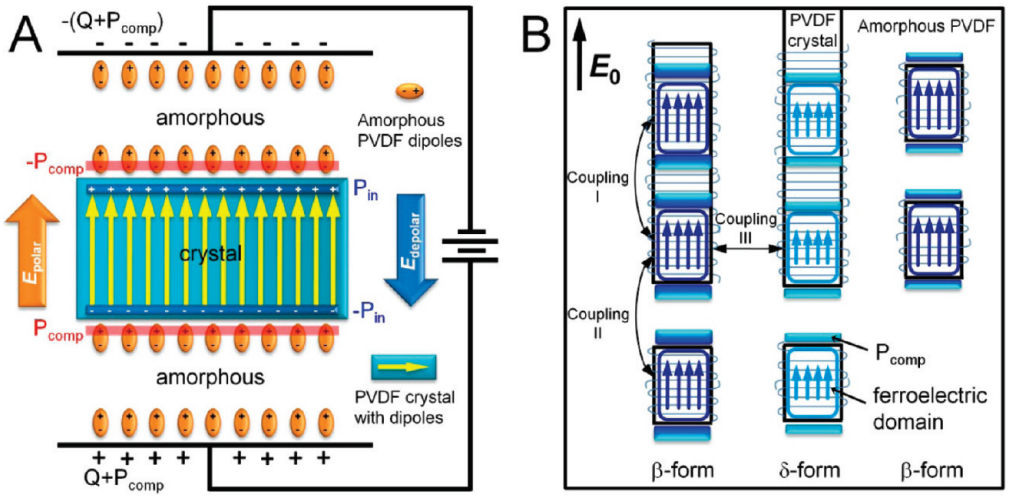

Figure 13. Schematic representations of (A) an electrically poled ferroelectric PVDF crystal sandwiched between two amorphous layers and (B) many electrically poled ferroelectric PVDF crystals in an amorphous matrix, showing different coupling interactions among ferroelectric domains. The chain direction in the lamellar crystals is perpendicular to the film normal (or the external electric field).

is a local electric field in the ferroelectric crystal, the relative permittivity of the crystal should not appear in the denominator. The P_{in} in turn induces the polarization of the amorphous PVDF at the amorphous−crystalline interfaces, resulting in a compensation polarization (P_{comp}) outside the ferroelectric PVDF domain. The P_{comp} in amorphous PVDF is determined by the dipole density in the amorphous phase ($N_{0,am}$), the polarizability for amorphous PVDF (α_{am}), and the local electric field in the amorphous phase ($E_{L,am}$):[36]

$$P_{comp} = N_{0,am}\alpha_{am}E_{L,am} \tag{2}$$

Note that P_{in} may not equal P_{comp} especially during dynamic (i.e., nonequilibrium) poling processes. Based on the serial capacitor model in Figure 13A (or see the equivalent serial model in Figure S1 in the Supporting Information), the local polarization field for the PVDF crystal is imposed from the charges on the electrodes and can be defined as[36,37]

$$E_{pol} = \frac{D}{\varepsilon_0} = \frac{Q + P_{comp}}{\varepsilon_0} \tag{3}$$

where Q is the charge density induced in the vacuum, i.e., $Q = \varepsilon_0 E$. Again, E_{pol} is a local electric field and the relative permittivity should not appear in the denominator.

The switching of a dipole in the crystalline PVDF does not depend on the macroscopic nominal electric fields in either the amorphous (E_{am}) or the crystalline (E_{cryst}) PVDF:

$$E_{am} = \frac{Q + P_{comp}}{\varepsilon_0 \varepsilon_r^{am}(E)} \tag{4}$$

$$E_{cryst} = \frac{D}{\varepsilon_0 \varepsilon_r^{cryst}(E)} = \frac{Q + P_{comp}}{\varepsilon_0 \varepsilon_r^{cryst}(E)} \tag{5}$$

where $\varepsilon_r^{am}(E)$ and $\varepsilon_r^{cryst}(E)$ are the relative permittivity of the amorphous and crystalline PVDF as a function of the electric field, respectively. [Note that $\varepsilon_r^{am}(E)$ should be a linear dielectric constant and $\varepsilon_r^{cryst}(E)$ should be a nonlinear dielectric constant.] Instead, dipole switching depends on the local electric field in the crystal ($E_{L,cryst}$), which has at least three sources: (i) E_{pol} (positive), (ii) E_{depol} (negative), and (iii) other contributions from dipoles nearby.[36] If we consider that contributions from other dipoles nearby can cancel out due to a random orientation, contribution iii may be neglected. Then, the local electric field largely depends on the competition between E_{pol} and E_{depol}, which is determined by the relationship between P_{in} and $Q + P_{comp}$. Upon a forward poling, $Q + P_{comp} > P_{in}$ and thus $E_{pol} > E_{depol}$. Crystalline dipoles become oriented along the external electric field. During a reverse poling process, two scenarios can take place. When the previous forward poling field is relatively low, both E_{depol} and E_{pol} decrease with decreasing the external electric field upon reverse poling. At a certain point,

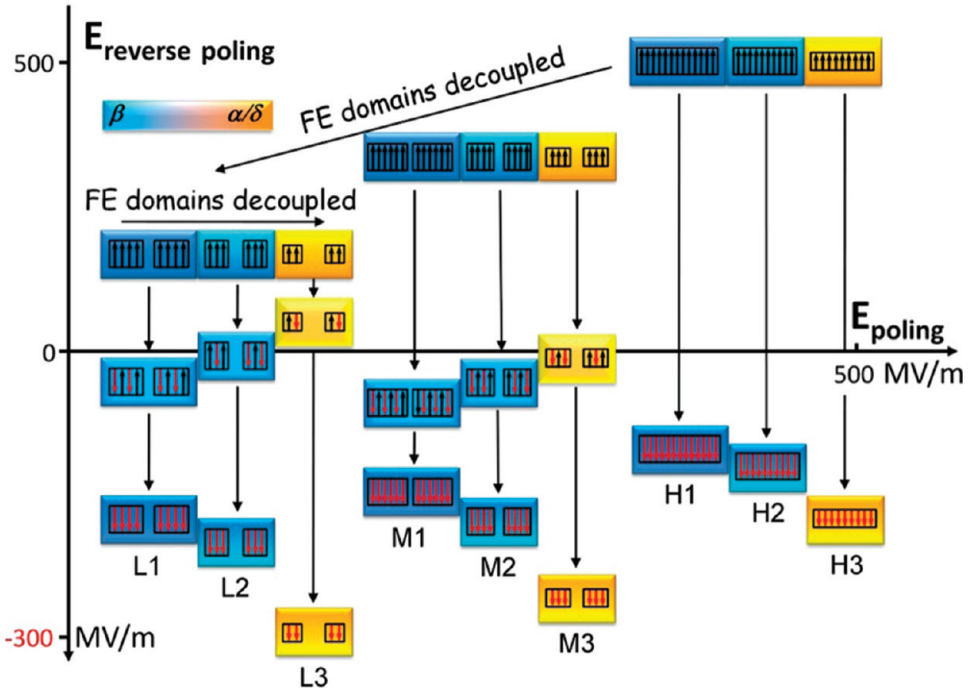

Figure 14. Schematic representation of the dipole reorientation, i.e., two-step dipole reversals, during reverse poling processes (the vertical axis) after prior forward poling (the horizontal axis). Polymorphism is represented as a blue color for the β-form and an orange color for the α/δ-form. PVDF lamellar crystals are represented as colored boxes, while ferroelectric domains are represented as black rectangles inside the crystals. Dipoles are represented by arrows. However, neighboring arrows do not represent neighboring dipoles in a crystalline unit cell because the antiparallel β-crystal unit cell does not exist.

$P_{in} > Q + P_{comp}$ and $E_{depol} > E_{pol}$, and thus an antiferroelectric-like behavior is achieved. However, when the previous forward poling field is high, $P_{in} < Q + P_{comp}$ and E_{depol} turns out to be always lower than E_{pol}. Therefore, the antiferroelectric-like behavior is not observed; instead, the normal ferroelectric behavior is seen.

When many ferroelectric crystals are poled by an external electric field, ferroelectric domain coupling is realized via induced polarizations (i.e., P_{comp}) from the media (either amorphous or crystalline PVDF) between the domains.[18,38,39] Different situations are shown in Figure 13B. First, there are three types of coupling interactions: I (within the ferroelectric crystal), II (between ferroelectric crystals but along the external field direction), and III (between ferroelectric crystals but perpendicular to the external field direction). Note that for the coupling interaction I the P_{comp} is induced by neighboring ferroelectric domains inside the crystal (i.e., the ferroelectric domain is smaller than the PVDF crystal; see the top left and top middle panels in Figure 13B), and it may be defined as[36]

$$P_{comp} = N_{0,cryst}\alpha_{cryst}E_{L,cryst} \quad (6)$$

where $N_{0,cryst}$ is the dipole density in the crystalline phase, α_{cryst} the polarizability for crystalline PVDF, and $E_{L,cryst}$ the local electric field in the crystal. Because the coupling interactions are anisotropic,[40] coupling III is much weaker than couplings I and II. For ferroelectric polymers, the α_{cryst} is generally higher than the α_{am}, and thus coupling I is stronger than coupling II (see the left panel in Figure 13B). Second, dipole moments in β-crystals are larger than those in δ-crystals, and thus the local electric field is higher near β-domains than δ-domains. As a result, the P_{comp} induced by β-domains are higher than that by δ-domains. Therefore, the coupling interactions (I + II) among β-domains are stronger than those among δ-domains (see left and middle panels of Figure 13B). Third, when the crystallite size is very small and just contains one ferroelectric domain (right panel of Figure 13B), coupling I interaction disappears, and thus the overall coupling interaction become weaker than the situation where a crystallite contains multiple domains at the same electric field.

On the basis of the results from Figures 10 and 11 and the understanding of ferroelectric domain coupling and competition between polarization and depolarization fields from Figure 13, effects of poling fields (both forward and reverse), polymorphism, and crystallite size on dipole switching/reorientation behaviors are summarized and explained in Figure 14. At low forward poling fields (ca. <200 MV/m; see panels L1−L3 in Figure 14), ferroelectric domains with positively aligned dipoles just nucleated and thus were small. The coupling among these small aligned ferroelectric domains is weak. First, we will discuss the effect of polymorphism on the dipole reversal, assuming that the crystallite size is similar (see panels L2 and L3 in Figure 14 and compare left and middle panels in Figure 13). Because the coupling among β-domains is stronger than that among δ domains, P_{comp} induced by β-domains is higher than P_{comp} induced by δ-domains. Upon reverse poling, more negative Q (i.e., more negative external field) is needed for β-domains (panel L2 in Figure 14) than for δ-domains (panel L3 in Figure 14) to meet the requirement of $Q + P_{comp} < P_{in}$ for the first-step dipole reversal. Again, because of the stronger coupling (or larger P_{comp}) among β-domains than among δ-domains, less negative Q (i.e., less negative external field) is necessary for β-domains (panel L2 in Figure 14) than for δ-domains (panel L3 in Figure 14) to meet the requirement of $Q + P_{comp} > P_{in}$ for the second-step dipole reversal. Second, we will discuss the effect of crystallite size, assuming the same β-form (see panels L1 and L2 in Figure 14 and compare the left and right panels in Figure 13). When the crystallite size is small, the coupling among ferroelectric domains is weak, which tends to result in lower P_{comp}. Therefore, less negative Q is required for the first-step dipole reversal and more negative Q is required for the second-step dipole reversal. As a result, the first-step dipole reversal appears at a low reverse field in small β-crystallites, and the second-step dipole reversal in small

crystals (L2 in Figure 14) occurs at a higher reverse field than in large crystals (L1 in Figure 14).

At medium forward poling fields (ca. 200−300 MV/m, see panels M1−M3 in Figure 14), ferroelectric domains have grown to medium sizes with more positively aligned dipoles. The coupling among neighboring ferroelectric domains becomes stronger and results in a higher P_{comp} due to a higher local field. Therefore, similar situations to those at low forward poling fields take place; more negative Q (or external field) is required for the first-step dipole reversal and less negative Q (or external field) is required for the second-step dipole reversal (panels M1−M3 in Figure 14) during reverse poling when the polymorphism changes from α/δ to β and crystallite size increases from small to large.

At even higher forward poling fields (ca. >400 MV/m; see panels H1−H3 in Figure 14), ferroelectric domains have well-developed with large domain sizes and the dipole orientation approaches saturation. The coupling between neighboring ferroelectric domains is so strong that $Q + P_{comp}$ becomes always higher than P_{in}. The first-step dipole reversal vanishes, and the second-step dipole reversal occurs at a less negative reverse field (panels H1−H3 in Figure 14) as the polymorphism changes from α/δ to β and the crystallite size increases from small to large.

From the above discussion, we consider that the antiferroelectric-like behavior should be a universal phenomenon for ferroelectric polymers, not specific to a particular condition. In other words, whenever P_{comp} (or $Q + P_{comp}$) is low, E_{depol} can be higher than E_{pol} during reverse poling, and the antiferroelectric-like behavior will happen. On the basis of our results, the value of P_{comp} is determined by the polarizability and the local electric field (see eqs 2 and 6). The polarizability and local electric field are actually closely related to the dipole moment per chain per repeat unit (polymorphism), dipole mobility, and ferroelectric domain size (limited by the crystallite size). For example, the antiferroelectric-like behavior cannot be observed in pure β-form PVDF at room temperature because the P_{comp} is so high that the field required for antiferroelectric-like behavior may be even lower than the second-step dipole reversal (i.e., the coercive field during reverse poling where $D = 0$). However, the antiferroelectric-like behavior can be observed in several cases with reduced P_{comp} comparing to the pure β-form PVDF. First, when the temperature was below −60 °C, the polarizability decreased due to a decrease in dipole mobility in amorphous PVDF and P_{comp} was much smaller than that at room temperature. As a result, the antiferroelectric-like behavior was observed in β-form PVDF at low temperatures.[29] Second, P_{comp} can be reduced by decreasing the dipole moment per chain per repeat unit. In fact, the antiferroelectric-like behavior was observed in PVDF and its copolymers with mixed β- and α/δ-crystals (films in this work) and in P(VDF-*co*-trifluoroethylene) [P(VDF−TrFE)] copolymers with 50−70 mol % TrFE.[30,31] Note that the dipole moment per chain per repeat unit in α/δ-form PVDF and P(VDF−TrFE) are 1.62[41] and 1.05 D, respectively, smaller than that of 2.1 D for β-form PVDF.[42,43] Finally, P_{comp} can also be reduced by small ferroelectric domain sizes via confining them in small crystallites, and film B is a good example (Figure 6).

At last, we noted that comparing the P(VDF−HFP) film B with the PVDF film A for the crystallite size effect may not be the best choice because different molecular weights/molecular weight distributions and, in particular, different head-to-head/tail-to-tail (HHTT) contents may cause differences in crystalline (e.g., melting point and crystal modification)[3] and thus ferroelectric behaviors. For example, for PVDF with more than 12% HHTT content, β- instead of α-crystals were obtained. Based on ^{19}F NMR data (not shown), the P(VDF−HFP) sample had an HHTT content of 5.5% in the PVDF sequence, which was similar to that of the PVDF homopolymer (e.g., 5−6% for Kynar samples).[3] Therefore, we consider that the effect of HHTT content should not be a major concern for comparing film B [P(VDF−HFP)] with film A (PVDF). The best choice for studying crystallite size effect would be to compare the same sample [either P(VDF−HFP) or PVDF] with different crystallite sizes, while keeping the same crystal orientation and polymorphism. However, there had been technical difficulty in experiments. First, mechanical stretching would always produce small crystallize sizes, no matter how large the crystallize size we could obtain for unoriented P(VDF−HFP) samples by either slow cooling or isothermal crystallization from the quiescent melt. Second, for the PVDF homopolymer, no matter how fast we quenched the sample from the melt into ice/water, oriented, edge-on, small β-crystals could not be obtained even after mechanical stretching. For example, for quickly quenched PVDF homopolymer from the melt, the crystallite sizes were still large after uniaxial stretching; $D_{(110)\alpha}$ = 30 nm and $D_{(110/220)\beta}$ = 24 nm (data not shown). Therefore, we chose to compare the small β-crystals in P(VDF−HFP) with the large β-crystals in biaxially oriented PVDF. In the future, we will design new experiments to obtain oriented, edge-on, large β-crystals in the same P(VDF−HFP) sample to compare with film B, which has oriented, edge-on, small β-crystals.

Conclusions

In summary, different polymorphisms and crystallite sizes were obtained in PVDF and P(VDF−HFP) films by using different film preparation/processing methods. Their effects on the dipole reorientation behavior and electric energy storage/release were studied by high field $D-E$ loop measurements. It was found that the coupling interactions among ferroelectric domains were facilitated by a high β content and a large crystallite size. As a result, a higher E_{pol} (or $Q + P_{comp}$) than E_{depol} (or P_{in}) was achieved, and dipoles in the highly coupled ferroelectric domains could be easily polarized, resulting in a high dielectric constant and a high stored energy density. From a pure electric energy storage point of view, transverse β-crystals were more preferable than transverse α/δ-crystals. However, electric energy discharge required that the polarized dipoles quickly switch back to an antiferroelectric-like (or a random) state upon removal of the poling field. Obviously, this was unlikely for highly coupled ferroelectric domains. A viable solution is to nanoconfine the β ferroelectric domains to reduce the coupling and thus P_{comp}. Two methods could be employed. First, when the poled ferroelectric domains are just nucleated with limited growth at relatively low forward poling fields (e.g., 100−250 MV/m), ferroelectric domains are "nanoconfined" due to a low nucleation density. As a result, an easy reversal of weakly coupled dipoles to the antiferroelectric-like state can be achieved (see panels L1−L3 and M1−M3 in Figure 14). However, this is not very practical for high energy density capacitors because they often operate at high fields (e.g., ≥300 MV/m). Second, ferroelectric domains can be physically confined by small (or nanosized) crystallites with discontinuous boundaries, where the ferroelectric domain coupling (or P_{comp}) is weak enough to induce an easy dipole reversal upon reverse poling. This is the reason why film B showed the highest discharged electric energy density among all films. This study can provide us fundamental insights into the dipole reorientation mechanism and its implication for the practical application of ferroelectric polymers for advanced high energy density dielectric film capacitors.

Acknowledgment. The authors are indebted to Professor Takeo Furukawa at Tokyo University of Science and Professors Jerome Lando and Donald Schuele at Case Western Reserve

University for helpful discussions. This work was supported by ONR (N00014-05-1-0338) and NSF (DMR-0907580).

Supporting Information Available: The equivalent serial capacitor model. This material is available free of charge via the Internet at http://pubs.acs.org.

References and Notes

(1) Lovinger, A. J. *Science* **1983**, *220*, 1115–1121.
(2) Karawasa, N.; Goddard, W. A., III *Macromolecules* **1992**, *25*, 7268–7281.
(3) Tashiro, K. Crystal Structure and Phase Transition of PVDF and Related Copolymers. In *Ferroelectric Polymers: Chemistry, Physics, and Applications*, 1st ed.; Nalwa, H. S., Ed.; Dekker: New York, 1995; pp 63−182.
(4) Lu, Y.; Claude, J.; Neese, B.; Zhang, Q. M.; Wang, Q. *J. Am. Chem. Soc.* **2006**, *128*, 8120–8121.
(5) Lu, Y.; Claude, J.; Zhang, Q. M.; Wang, Q. *Macromolecules* **2006**, *39*, 6962–6968.
(6) Xu, H.; Shen, D.; Zhang, Q. *Polymer* **2007**, *48*, 2124–2129.
(7) Jow, T. R.; Cygan, P. J. *J. Appl. Phys.* **1993**, *73*, 5147–5151.
(8) Chu, B.; Zhou, X.; Ren, K.; Neese, B.; Lin, M.; Wang, Q.; Bauer, F.; Zhang, Q. M. *Science* **2006**, *313*, 1887–1887.
(9) Zhou, X.; Chu, B.; Neese, B.; Lin, M.; Zhang, Q. M. *IEEE Trans. Dielectr. Electr. Insul.* **2007**, *14*, 1133–1138.
(10) Zhou, X.; Zhao, X.; Suo, Z.; Zou, C.; Runt, J.; Liu, S.; Zhang, S.; Zhang, Q. M. *Appl. Phys. Lett.* **2009**, *94*, 162901.
(11) Mizutani, T.; Yamada, T.; Ieda, M. *J. Phys. D: Appl. Phys.* **1981**, *14*, 1139–1147.
(12) Starkweather, J., H. W.; Avakian, P.; Matheson, R. R.; Fontanella, J. J.; Wintersgill, M. C. *Macromolecules* **1992**, *25*, 6871–6875.
(13) Tan, Q.; Irwin, P.; Cao, Y. *IEEJ Trans. FM* **2006**, *126*, 1152–1159.
(14) MacDougall, F.; Ennis, J.; Yang, X. H.; Seal, K.; Phatak, S.; Spinks, B.; Keller, N.; Naruo, C.; Jow, T. R. In *Large High Energy Density Pulse Discharge Capacitor Characterization*; IEEE International Pulsed Power Conference, Monterey, CA, 2005; pp 1−4.
(15) Ranjan, V.; Yu, L.; Nardelli, M. B.; Bernholc, J. *Phys. Rev. Lett.* **2007**, *99*, 047801.
(16) Guan, F.; Yuan, Z.; Shu, E. W.; Zhu, L. *Appl. Phys. Lett.* **2009**, *94*, 052907.
(17) von Seggern, H.; Fedosov, S. N. *Appl. Phys. Lett.* **2002**, *81*, 2830–2832.
(18) Stephanovich, V. A.; Luk'yanchuk, I. A.; Karkut, M. G. *Phys. Rev. Lett.* **2005**, *94*, 047601.
(19) Chen, Q.; Wang, Y.; Zhou, X.; Zhang, Q. M.; Zhang, S. *Appl. Phys. Lett.* **2008**, *92*, 142909.
(20) Guan, F.; Pan, J.; Wang, J.; Wang, Q.; Zhu, L. *Macromolecules* **2010**, *43*, 384–392.
(21) Klein, R. J.; Runt, J.; Zhang, Q. M. *Macromolecules* **2003**, *36*, 7220–7226.
(22) Kobayashi, M.; Tashiro, K.; Tadokoro, K. *Macromolecules* **1975**, *8*, 158–171.
(23) Kanai, T.; Campbell, G. A. *Film Processing*; Hanser/Gardner Publications: Cincinnati, 1999.
(24) Young, R. J.; Lovell, P. A. *Introduction to Polymers*, 2nd ed.; Nelson Rhornes: Cheltenham, 1991.
(25) Matsushige, K.; Nagata, K.; Imada, S.; Takemura, T. *Polymer* **1980**, *21*, 1391–1397.
(26) Zhu, L.; Calhoun, B. H.; Ge, Q.; Quirk, R. P.; Cheng, S. Z. D.; Thomas, E. L.; Hsiao, B. S.; Yeh, F.; Liu, L.; Lotz, B. *Macromolecules* **2001**, *34*, 1244–1251.
(27) Furukawa, T.; Lovinger, A. J.; Davis, G. T.; Broadhurst, M. G. *Macromolecules* **1983**, *16*, 1885–1890.
(28) Furukawa, T.; Nakajima, K.; Koizumi, T.; Date, M. *Jpn. J. Appl. Phys.* **1987**, *26*, 1039–1045.
(29) Furukawa, T.; Date, M.; Fukada, E. *J. Appl. Phys.* **1980**, 1135–1141.
(30) Takahashi, Y.; Kodama, H.; Nakamura, M.; Furukawa, T.; Date, M. *Polym. J.* **1999**, *31*, 263–267.
(31) Furukawa, T.; Takahashi, Y. *Ferroelectrics* **2001**, *264*, 1739–1748.
(32) Lu, Y.; Claude, J.; Norena-Franco, L. E.; Wang, Q. *J. Phys. Chem. B* **2008**, *112*, 10411–10416.
(33) Charnaya, E. V.; Pirozerskii, A. L.; Tien, C.; Lee, M. K. *Ferroelectrics* **2007**, *350*, 75–80.
(34) Sarjeant, W. J.; Zirnheld, J.; MacDougall, F. W. *IEEE Trans. Plasm. Sci.* **1998**, *26*, 1368–1392.
(35) Wolak, M. A.; Pan, M. J.; Wan, A.; Shirk, J. S.; Mackey, M.; Hiltner, A.; Baer, E.; Flandin, L. *Appl. Phys. Lett.* **2008**, *92*, 113301.
(36) Blythe, A. R. *Electrical Properties of Polymers*; Cambridge University Press: Cambridge, 1979; pp 15−37.
(37) Black, C. T.; Farrell, C.; Licata, T. J. *Appl. Phys. Lett.* **1997**, *71*, 2041–2043.
(38) Samara, G. A. *J. Phys.: Condens. Matter* **2003**, *15*, R367–R411.
(39) Zhou, Y.; Shin, F. G. *J. Appl. Phys.* **2006**, *100*, 024101.
(40) Hooton, J. A.; Merz, W. J. *Phys. Rev.* **1955**, *98*, 409–413.
(41) Takakubo, M.; Teramura, K. *J. Polym. Sci., Part A: Polym. Chem.* **1989**, *27*, 1897–1905.
(42) Hayashi, S. I.; Imamura, A. *J. Polym. Sci., Part B: Polym. Chem.* **1992**, *30*, 769–773.
(43) Fukada, E.; Furukawa, T. *Ultrasonics* **1981**, *19*, 31–39.